

RESEARCH ARTICLE

# Direct and quantitative assessments of near-infrared light attenuation and spectroscopic detection depth in biological tissues using surface-enhanced Raman scattering

Li Lin<sup>1,2</sup>  · Haoqi He<sup>1</sup> · Ruiyang Xue<sup>2</sup> · Yumin Zhang<sup>1</sup> · Ziwen Wang<sup>2</sup> · Shuming Nie<sup>2</sup> · Jian Ye<sup>1,3,4</sup> 

Received: 24 February 2023 / Revised: 11 July 2023 / Accepted: 12 July 2023  
© The Author(s) 2023

## Abstract

Optical imaging and spectroscopic modalities are of broad interest for in-vivo molecular imaging, fluorescence guided cancer surgery, minimally invasive diagnostic procedures, and wearable devices. However, considerable debate still exists as to how deeply visible and near-infrared (NIR) light could penetrate normal and diseased tissues under clinically relevant conditions. Here we report the use of surface-enhanced Raman scattering (SERS) nanotags embedded in ex-vivo animal tissues for direct and quantitative measurements of light attenuation and spectroscopic detection depth at both the NIR-I and NIR-II spectral windows. SERS nanotags are well suited for this purpose because of their sharp spectral features that can be accurately differentiated from fluorescence and background emission. For the first time, the spectroscopic detection depth is quantitatively defined and measured as the maximal thickness of tissues through which the embedded SERS nanotags are still detected at a signal-to-noise ratio (SNR) of three (99.7% confidence level). Based on data from six types of fresh ex-vivo tissues (brain, kidney, liver, muscle, fat, and skin), we find that the maximum detection depth values range from 1–3 mm in the NIR-I window, to 3–6 mm in the NIR-II window. The depth values are largely determined by two factors – the intrinsic optical properties of the tissue, and the overall SNRs of the system without the tissue (system SNR, a result of nanotag brightness, instrument efficiency, and data acquisition parameters). In particular, there is an approximately linear-logarithmic relationship between the system SNR and maximum detection depth. Thus, the detection of hidden or occult lesions can be improved by three strategies – reducing tissue attenuation, minimizing background noise, and maximizing the system's performance as judged by SNR.

---

✉ Li Lin  
linli92@sjtu.edu.cn

✉ Shuming Nie  
nies@illinois.edu

✉ Jian Ye  
yejian78@sjtu.edu.cn

<sup>1</sup> State Key Laboratory of Systems Medicine for Cancer, School of Biomedical Engineering, Shanghai Jiao Tong University, Shanghai, P.R. China

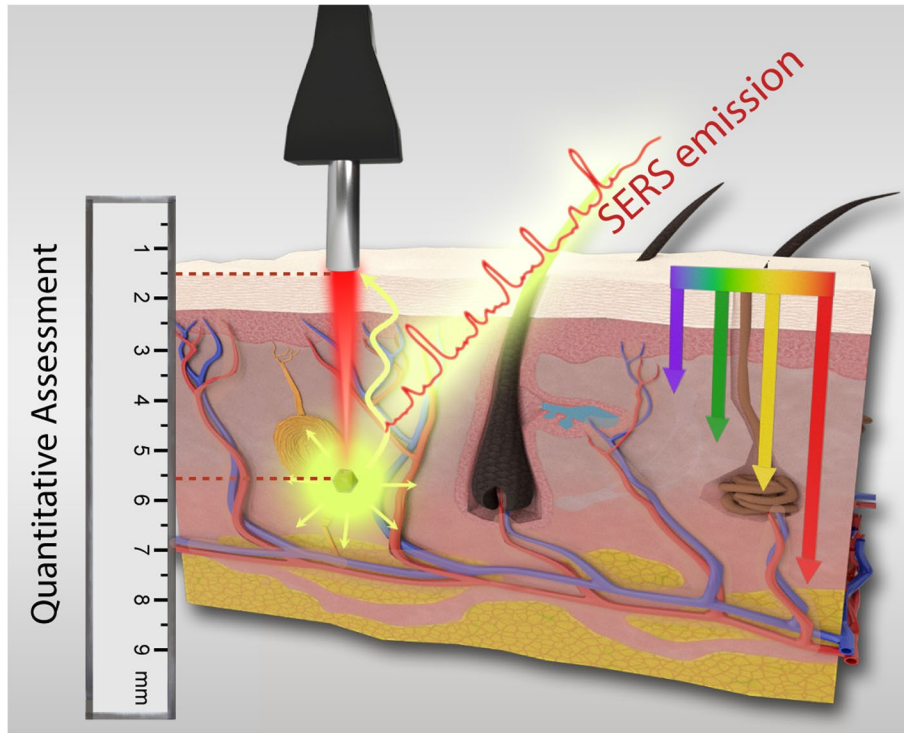
<sup>2</sup> Department of Bioengineering, University of Illinois at Urbana-Champaign, Illinois, USA

<sup>3</sup> Shanghai Key Laboratory of Gynecologic Oncology, Ren Ji Hospital, School of Medicine, Shanghai Jiao Tong University, Shanghai, P.R. China

<sup>4</sup> Institute of Medical Robotics, Shanghai Jiao Tong University, Shanghai, P.R. China



## Graphical Abstract



## Highlights

- The spectroscopic detection depth is quantitatively defined and measured as the maximal thickness of tissues through which the embedded Raman nanotags are detected at a signal-to-noise ratio of three.
- The intrinsic optical properties of the tissue and the system signal-to-noise ratio are the two deciding factors of signal penetration in bio-tissues.
- A generalized linear-logarithmic relationship is revealed between the system SNR and spectroscopic detection depth for each tissue.

**Keywords** Surface-enhanced Raman scattering · Near-infrared window · Biological detection · Detection depth

## Introduction

Recent advances in biomedical optics have had a profound impact on the diagnosis and treatment of many human diseases. In particular, optical imaging and spectroscopic modalities have played an important role in surgical navigation and guidance, allowing real-time visualization of tumor margins and sensitive detection of metastatic lymph nodes. However, a major concern is still the limited penetration of photons in turbid biological tissues [1]. As the photons travel through the tissue, absorption and scattering together cause the light beams to broaden and attenuate, and meanwhile autofluorescence leads to the increase of noises [2]. Extensive efforts have been made to address this

problem, including extending the excitation light to longer wavelengths [3]. The widely applied NIR-I (Near-infrared-I) window (650–950 nm in wavelength) shows reduced tissue scattering and absorption compared to the visible spectrum (400–700 nm in wavelength) [3]. Further reduction in scattering, absorption and autofluorescence is observed at the NIR-II window (1000–1700 nm in wavelength), which allows deep-tissue detection with the improved signal-to-noise ratio (SNR), higher sensitivity and better spatial resolution [4, 5]. For example, fluorescence at the NIR-II window has been shown to penetrate a depth of more than 2 mm in mouse brain with a high resolution [6], and the ex vivo fluorescence penetration in chicken breast tissue was reported to be over 8 mm [4]. In general, high penetration in

biological tissues is required to achieve high quality *in vivo* bioimaging or detections. The spectroscopic detection depth in tissues serves as a strong indicator to evaluate the detection performance in tissues.

Although substantial attention has been paid to improve tissue penetration, not many data of the precise detection depths at the NIR window are available in current literature. These data depend on the sample preparation, measurement process, tissue property and data analysis algorithm. The idea of quantitative *ex vivo* assessments on maximum detection depths is underexplored with the lack of systematic evaluation data. As far as we know, various procedures have been independently used by different research groups to estimate the maximum detection depth [7–9]. For instance, the assessments were conducted with the imaging agents injected into tissues phantoms [7], or coated on a solid surface covered by tissue [10], or filled in a container embedded in tissues [4, 11]. The criteria of effective signals were also varying, which includes directly reading out the peak heights [11, 12], evaluating the ratio between two peaks [10], or adopting the retrieved information by principal component analysis [13]. These assessments are expected to provide new perspectives to a variety of through-tissue detection implementations ranging from *in vivo* molecular imaging to spectroscopic analysis of biological tissues. But the inconsistency of measurement methods and criteria makes it challenging to directly compare results among different independent studies across this field. The quantitative studies, such as the tissue attenuation and penetration at the NIR-I and NIR-II window are yet to be reported. The fundamental questions regarding the tissue optical properties, such as the how the tissue attenuation is affected by the measurement parameters (such as laser power and integration time) at the NIR window also remained unclear.

Here, this challenge is addressed experimentally with our systematic assessments of quantitative spectroscopic detection depth presented by using surface-enhanced Raman scattering (SERS) nanotags. Raman spectroscopy is the fingerprint spectrum induced by the inelastic scattering of the substances upon the interaction with incident light. Unlike the fluorescence spectrum that is broad (> 50 nm of peak width) and may be interfered by the tissue background, Raman peaks are intrinsically narrow (1–2 nm), which can be well discriminated from the endogenous chemicals. SERS can enhance the normal Raman spectral intensity by over up to  $10^1$ , providing exceptional sensitivity and specificity [14]. SERS nanotags, are promising imaging contrast agents, composed of the plasmonic substrate and Raman reporter molecules. They can be introduced *in vivo* via intravenous injection or local injection, and then accumulate at the tumor site through either passive transportation or active targeting; and the lesion location can be determined by detecting the characteristic spectrum of SERS nanotags [15]. So far,

SERS nanotags have been reported for the tumor diagnosis, tumor boundary identification, surgical guidance, and multi-mode theragnostic applications, holding a promise for intraoperative imaging with its intrinsic fingerprints [16–18]. SERS nanotags at the NIR-II window were also explored, with the ability to detect objects buried in deeper biological tissues [11, 12, 19, 20]. The SERS nanotags are bright, photo-stable, with characteristic peaks, well suitable for the quantitative assessments of spectroscopic detection depth properties [12].

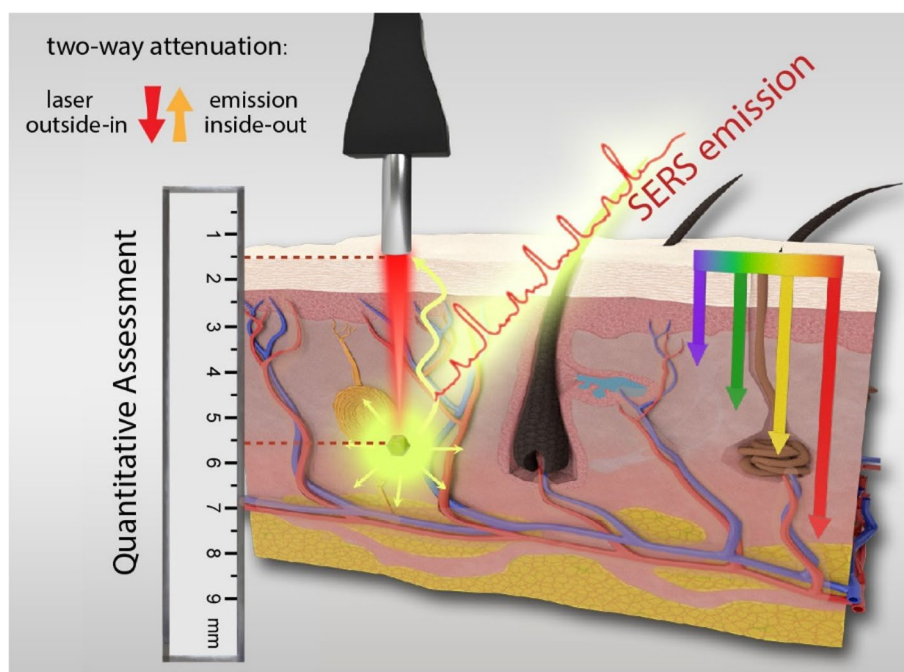
In this work, we quantitatively evaluated tissue attenuation and penetration at the NIR window with the use of SERS nanotags. We started the assessments by defining the detection depth based on the spectral SNR. During a successful through-tissue detection, the optical information is attenuated in propagation processes of both laser and emission (Fig. 1). For the first time, the term ‘spectroscopic detection depth’ has been quantitatively defined and measured as the maximum thickness of biological tissues through which the embedded SERS nanotags are still detected at a SNR of three (99.7% confidence level). The wavelength-dependent tissue background interferences and signal attenuations were compared between NIR-I (785 nm) and NIR-II (1064 nm) window. The weakened tissue background interference at 1064 nm demonstrated the superiority of NIR-II window in deep-tissue detections. A clear linear-logarithmic relationship between the SNR of the signal source and the detection depth was observed, which opened the possibility to predict the detection depth with known brightness of imaging agents. Using the similar assessment procedure, we have also investigated the fluorescence imaging depths on a commercial image-guided surgery system. To the best of our knowledge, this is the first report on the quantitative direct assessments of spectroscopic detection depth at the NIR window. This work provides a set of systematic assessment data as fundamental information for the design and implementation of *in vivo* SERS intraoperative applications.

## Results

### Setup and laser focus optimization

We presented the concept of quantitative assessments and the setup to evaluate NIR on spectroscopic detection depth on *ex-vivo* tissues with SERS. To mimic the clinical situation where the SERS Nanoparticles (NPs) were accumulated at the lesion within the biological tissues, we made a SERS gel (served as a lesion phantom tagged by the SERS NPs) and covered it with a layer of biological tissue, and a handheld Raman probe was utilized on the top to excite and collect Raman signals (Fig. 2a). The successful through-tissue detection is made via two steps: (1) the outside-in

**Fig. 1** Quantitative assessments of spectroscopic detection depth. The SERS gel is served as a phantom lesion, i.e., like a lesion tagged by SERS nanotags. In practical usage, SERS nanotags are injected in vivo, and accumulate at the lesion site. The laser illumination excites the Raman photons of SERS nanotags. Both the laser and Raman emission are attenuated during the transportation in tissues



propagation of incident radiation by a distance to excite the Raman-active signal sources; and (2) the inside-out propagation of scattered Raman photons through the same distance to be collected by the detector (see Fig. 1). The optical information is attenuated in both processes. Therefore, the spectroscopic detection depth is quantified as the largest thickness of tissues covering on a signal source, from which an effective signal can still be traced by the detector.

To make SERS gels, Au@Ag SERS NPs were firstly synthesized according to our previous protocols [21, 22], with a petal-like Au core, a Ag shell and a Raman molecule layer hidden in between. TEM images clearly show the rough surface of Au cores as well as the smooth morphology after Ag shell coating for Au@Ag SERS NPs (Fig. 2b). The UV–Vis spectrum of the Au NPs shows a resonant peak at 596 nm, well corresponding to the plasmon resonance of Au nanomaterials (Fig. 2c). After Ag shell coating, the NPs show two resonant peaks at 551 and 435 nm, confirming the successful coating of Ag shell. Here, 4-nitrobenzenethiol (4-NBT) was adopted as the Raman reporter molecules. The core–shell structure has proven to be able to protect the embedded Raman reporters from desorption or being interfered with particle aggregates, rendering excellent signal reproducibility for this assessment study [23]. Here, we have demonstrated that the NPs have distinguished Raman response even with a low concentration of 1 pM (Fig. 2d); they also show high detection sensitivity at the NIR-II window, as well as good signal stability and storage stability (Fig. S1).

The SERS gels were prepared by mixing the agarose solution and SERS NP colloids; after the mixture cooled down, the gels with SERS response were formed. The concentration of SERS NPs can be tuned to form SERS gels with

different brightness (Fig. S2). Since the NPs were dispersed in a liquid phase during the cooling process of the mixture, in this way, we were able to attain the Raman-active material in a solid-state while maintaining the uniform dispersion of NPs. As shown in Fig. S3, we have repeated measured a SERS gel at 10 random surface positions with the intensity deviation of only 5.1%. The SERS NPs and SERS gel exhibit characteristic peaks at 1338 and 1575  $\text{cm}^{-1}$  (Fig. 2d), which corresponds to  $\text{NO}_2$  asymmetrical stretching and C = C stretching of 4-NBT, respectively [24]. The strongest mode of SERS gels near 1338  $\text{cm}^{-1}$  can be distinguishable from that of common biological tissues (Fig. S4).

Our quantitative assessments apply spectral SNR for investigation. To process the collected Raman spectra, their baselines are firstly corrected to remove the tissue autofluorescence background; then, the signal intensities near peak position (usually at  $1338 \pm 6 \text{ cm}^{-1}$ ) are calculated, and the noises are the standard deviation in a region without any Raman peak, for example, the region of 2000–2200  $\text{cm}^{-1}$  (Fig. 2d). Also, we notice that biological tissues have some response near 1338  $\text{cm}^{-1}$ , which may bring biases when we read the intensity from a mixed Raman spectra contributed by tissue covered SERS gels. Therefore, a simple subtraction of tissue Raman background is conducted to extract a real value of signal intensity: we measure the intensity ratio of 1338  $\text{cm}^{-1}$  to 1445  $\text{cm}^{-1}$  for Raman spectra collected on pure tissues, then the tissue contribution at 1338  $\text{cm}^{-1}$  in the mixed spectrum can be determined and subtracted (See Experimental section and Fig. S5).

Before our detection depth assessments, we conducted the optimization of the laser beam focal plane. With the



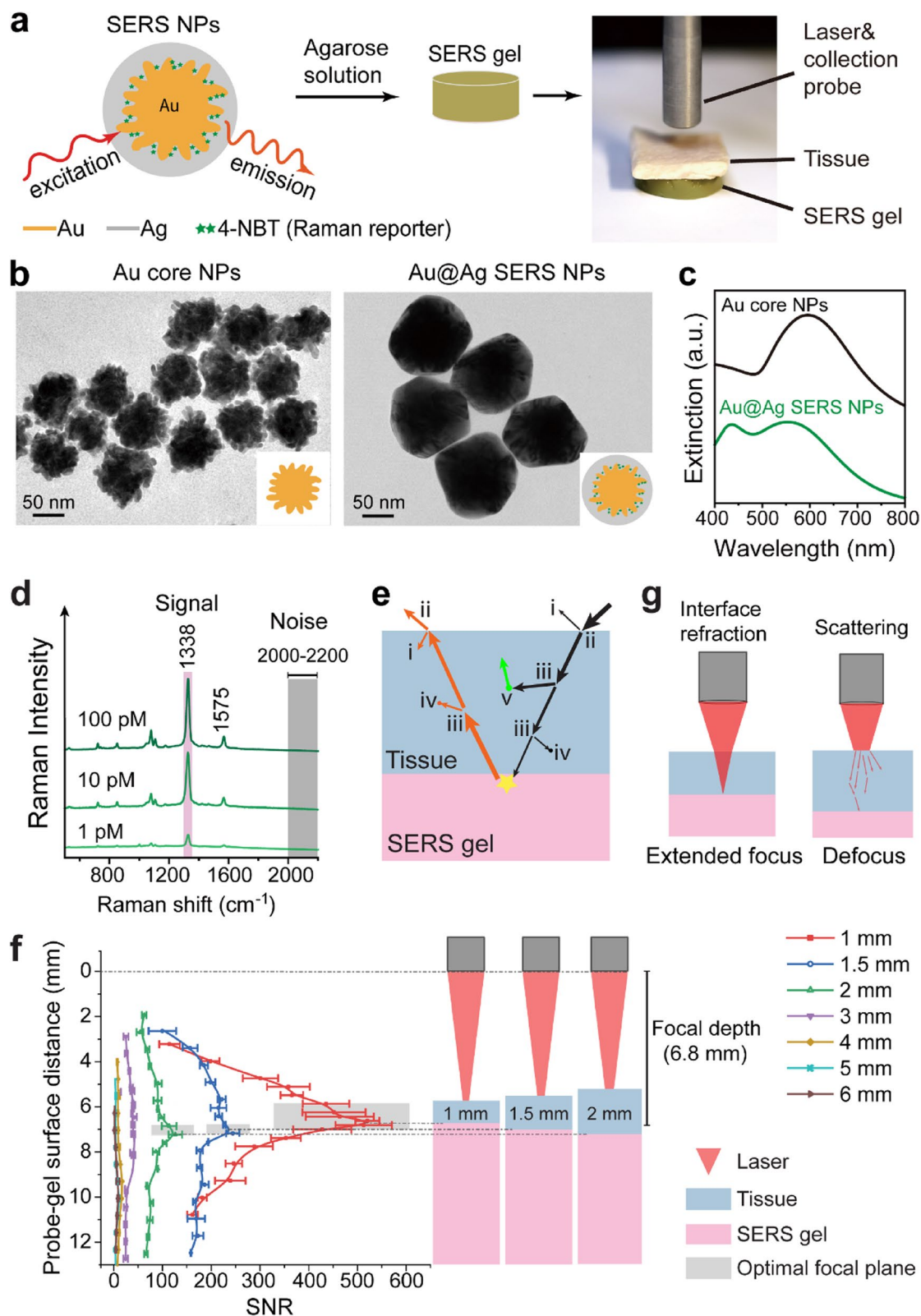


**Fig. 2** Setup and focal plane optimization. **a** Scheme of SERS gel preparation and setup. **b** TEM images and **(c)** UV-Vis spectra of Au core NPs and Au@Ag SERS NPs. **d** Raman spectra of 100, 10, and 1 pM SERS NP colloids under 785 nm excitation. **e** Signal attenuation during the penetrating outside-in and inside-out process: interface reflection (i), refraction (ii), scattering (iii), absorption (iv), auto-fluorescence (v). **f** The sequential SNR measurements at different probe-tissue distances on SERS gels covered with muscle layers of various thicknesses. The measurements adopted 200 mW power and 10 s integration time. The grey rectangles indicate the optimal focal planes. **g** Scheme of extended focus and defocus induced by tissue refraction or scattering

light-tissue interactions, a shift of laser focal plane may occur. Figure 2e shows the effects of light-tissue interactions [25]. First is reflection at the interface (Fig. 2e, i), such as the tumor-normal tissue interface for the in vivo environment; then comes refraction when light enters a tissue structure with a different refractive index (Fig. 2e, ii); there is also intense absorption of photon energy (Fig. 2e, iii) and multiple scattering of photons (Fig. 2e, iv); the autofluorescence is usually caused by the biological chromophores (Fig. 2e, v). Refraction and scattering are believed to induce the shift of laser focal plane, with the former bends light, and the latter randomizes the photon propagation direction. To determine that how these interactions would affect the focal plane and spectral intensity, our optimization procedure consists of the sequential acquisitions of Raman spectra on tissue-covered SERS gels while tuning the distance from the laser probe to gel surface. The focal depth and focal length of the laser beam was measured as 6.8 and 1.22 mm, respectively (Fig. S6). As a pure SERS gel was put under the laser beam, the strongest signal was obtained when the probe-gel distance is 4.9 mm (Fig. S7). This indicated that the optimal focus position of the pure SERS gel was  $\sim 1.9$  mm under the gel surface. This is reasonable, considering the common cases that the best laser focus is usually beneath the material surface. We then placed porcine muscle tissues with a thickness of 1–6 mm on the gel. As shown in Fig. 2f, with 1 mm of muscle tissue on top, the optimal probe-gel distance extends; the optimal focal plane is in the range of 5.91–6.89 mm, with the highest SNR obtained at 6.7 mm, very close to the focal length of 6.8 mm (Fig. 2f). Here, the optimal focal plane could be regarded as the distorted focal length of the laser beam, while it does not follow the Gaussian distribution due to the tissue light diffusion. With 2 or 3 mm muscle tissues on top, the curves become flatter, and the optimal focal planes further extend to 6.61–7.0 mm and 6.91–7.3 mm, respectively. We have also conducted the same measurements on fat and skin tissues (Fig. S8), and similar phenomenon were observed, i.e., the flattening of the SNR distribution profile as well as the tendency of the shift in optimal focal plane. As mentioned above, this could be explained by the interface refraction or tissue scattering. Refraction leads to an extended focal length, since the refractive index of tissues ( $n = 1.4$ ) is higher than that of the air ( $n = 1$ ); Multiple scattering of photons results in light diffuse and defocus (Fig. 2g). For thick tissues, scattering plays a more important role and can be described by the physical parameter, transport mean free path (TMFP). TMFP is the mean propagation distance that it takes for photons to lose relation to the propagation direction they had before entering the tissue. It takes into account the average angle by which photons are scattered in each scattering event. Depending on the tissue type and wavelength of operation, TMFP in muscle at the NIR region (650–1000 nm) was

reported to be  $\sim 1.1$  mm [26]. Therefore, for thick tissues of  $\geq 2$  mm, the incidence no longer follows the shape of a Gaussian beam, and the SNR becomes less sensitive to the probe-gel distances (as shown in Fig. 2f). When the tissue thickness increases to 3–6 mm, it is hardly able to tell the optimal focal plane. All the measurements were repeatedly conducted at least 3 times on different batches of tissues and SERS gels. The above results demonstrated that the optimal probe-gel distances are close to the focal length. To ensure the consistency of measurements, in the following studies, we fixed the distances between probe and gel surface the same as the focal length.

### Quantitative assessments on tissue attenuation and penetration: NIR-I versus NIR-II

The tissue attenuation and penetration properties were firstly compared on six types of tissues (brain, kidney, liver, muscle, fat and skin) between the first and second NIR window (Fig. 3). The same batch of tissues and SERS gel was adopted for the measurements for both wavelengths. For better comparisons, we chose 200 mW power with 0.5–2 s integration time for 785 nm, and 450 mW power with 2–10 s integration time for 1064 nm, making the SERS gel to generate comparable spectral intensities at two wavelengths. Figure 3a and b shows the profile of normalized SNR versus tissue thickness. The curves in Fig. 3a and b can be fitted well using an exponential decay model ( $R^2$  over 0.99). We have also plotted these data using a logarithmic y-axis scale (Fig. S9), and they can be fitted well with a log-linear model. A reduced tissue attenuation can be observed at the NIR-II window: under 785 nm excitation, the normalized SNR is attenuated by 80–93% with 1-mm tissue, with the most transparent one as the muscle. As for the 1064 nm excitation, the corresponding attenuation is reduced to 66–85%. At the NIR-II window, the penetration of muscle and liver is the highest, while kidney remain the most turbid tissues for both wavelengths. The attenuation of biological tissues mainly determined by its scattering and absorption properties [27]. Generally, the hemoglobin in the blood cells increases the light absorption, and lipids add in light scattering [28, 29]. Fat and brain tissues are rich in lipids. We also notice that the attenuation rates for skin is not uniform for skin of less than 1 mm and over 1 mm. We attribute this to the natural skin structure. As skin is a heterogeneous tissue, consist of epidermis top layer, dermis layer, and subcutaneous tissue layer, these layers exhibit different optical properties. Generally, 1-mm skin is mostly the epidermis layer ( $\sim 0.3$ –1.5 mm). Our result shows that epidermis layer is easier to penetrate at 1064 nm, indicating that NIR-II window may be promising for sub-skin lesion detections. This may indicate that NIR-II window is promising for sub-skin lesion detections.

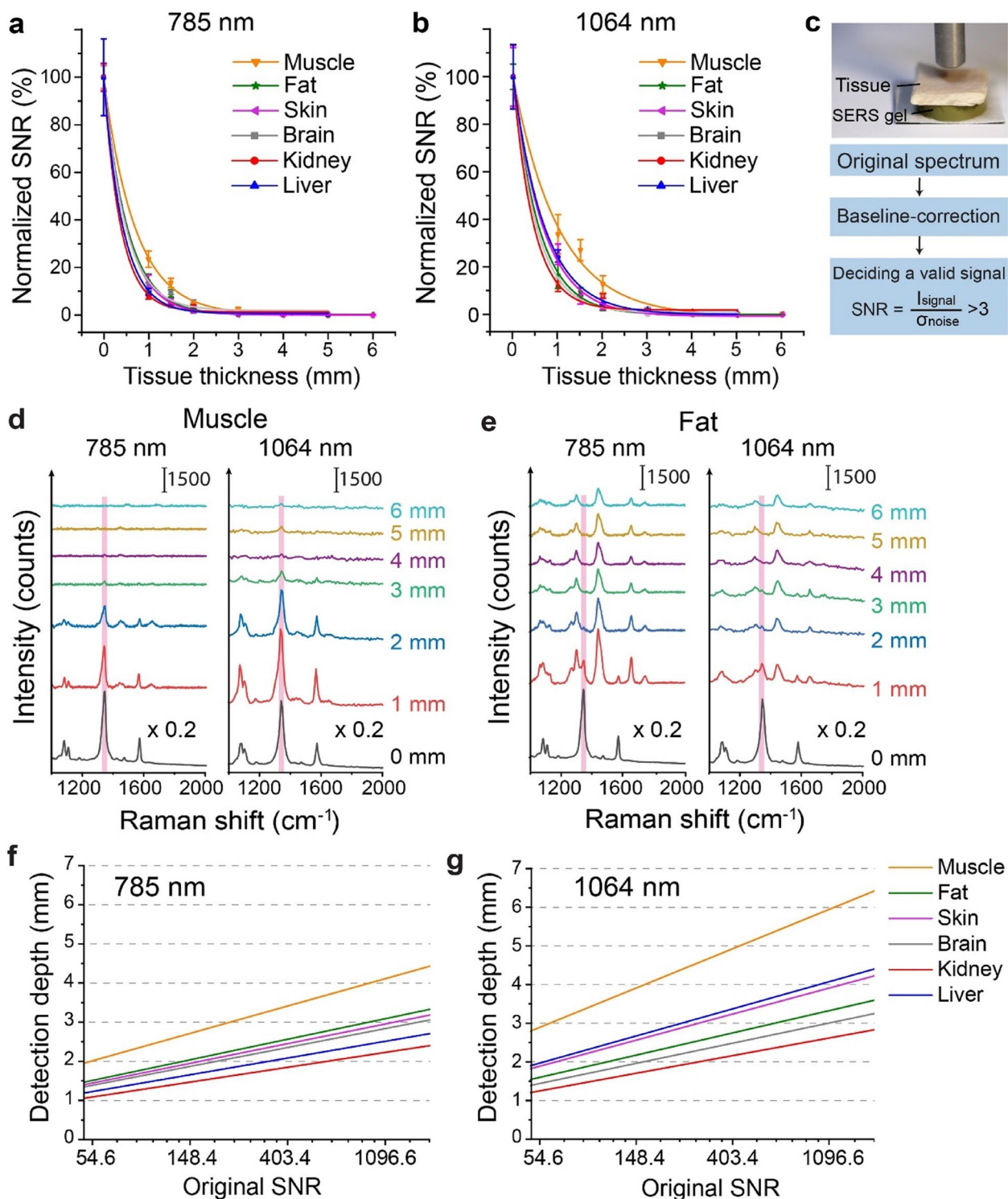


**Fig. 3** Depth-dependent attenuation of SERS signals in tissue at the NIR-I and NIR-II window. **a, b** The profile of normalized SNR versus tissue thickness at **(a)** 785 or **(b)** 1064 nm excitation. The R-squares of exponential fitting are all over 0.99. **c** Experimental setup and data processing procedure. **d, e** Representative Raman spectra of SERS gels covered with **(d)** muscle and **(e)** fat of different thicknesses. **f, g** The theoretical relationship between the original SNR and the maximum detection depth at the **(f)** NIR-I or **(g)** NIR-II window. The x-axis is displayed in the ln-scale

**Table 1** Tissue attenuation coefficients ( $\mu_{eff}$ ) of SNR at the NIR-I and NIR-II window, calculated according to Fig. 3. The data are presented as mean (SD)

Tissue types	$\mu_{eff}$ at 785 nm excitation	$\mu_{eff}$ at 1064 nm excitation
Brain	2.068 ± 0.205	1.917 ± 0.170
Kidney	2.629 ± 0.217	2.192 ± 0.329
Liver	2.333 ± 0.072	1.425 ± 0.046
Muscle	1.535 ± 0.082	0.982 ± 0.070
Fat	2.054 ± 0.205	1.737 ± 0.065
Skin	2.040 ± 0.102	1.483 ± 0.099

Tissue attenuation coefficient is the property of tissue itself, and is a measure of how much the incident beam is weakened by tissues it is passing through. Here we define  $\mu_{eff}$  as the effective attenuation coefficients of tissues, describing the fraction of the laser beam SNR or Raman signal SNR attenuated per unit thickness of the tissue. As the photons attenuate exponentially in regard to the tissue thickness, here we have

$$SNR_l = SNR_0 \cdot e^{-\mu_{eff} \cdot l} + c \quad (1)$$

where  $SNR_0$  represents the original SNR of the pure SERS gel,  $SNR_l$  represents the measured SNR with the tissue thickness of  $l$  on the SERS gel surface,  $c$  is a constant. The normalized SNR can be expressed as:

$$SNR_{normalized}(\%) = \frac{SNR_l}{SNR_0} = e^{-\mu_{eff} \cdot l} + \frac{c}{SNR_0} \quad (2)$$

Therefore, the fitted exponential decay model can be used to calculate  $\mu_{eff}$ . We repeated the measurements three times to get averaged data and deviations, as shown in Table 1. The direct comparison quantitatively demonstrates the reduced tissue attenuation at the NIR-II window. We have also compared our results to those measured using optical diffuse reflectance spectroscopy at the NIR-I window (See Supporting Information) [27]. The comparison indicates that the results on muscle and brain are close, while a relatively high difference exhibits for fat tissues. This may due to errors for different methods and measurements applied.

The representative spectra for muscle and liver tissue-covered SERS gels are shown in Fig. 3c and d. When covered by tissues, the signal peak (marked in pink) decreased dramatically and became unobservable with 5 mm muscle (or 2 mm fat) on top at 785 nm (Fig. 3d and e); In contrast, this peak is still exhibited with 5 mm muscle (or 3 mm fat) tissue on top at 1064 nm. The differences between 0 mm (original SERS gel) and 1 mm tissue covered at both wavelengths are the most prominent, indicating a better light tissue penetration at the NIR-II window.

We continued to make direct quantitative penetration assessments at both wavelengths. The spectral SNR was carefully calculated (Fig. 3c). Here, an effective Raman signal is defined based on the spectral SNR:

$$Effective\ SNR = \frac{I_{signal}}{\sigma_{noise}} \geq 3 \quad (3)$$

which indicates with > 99.7% confidence level that the signal is true rather than random noise. We defined the maximum detection depth ( $d$ ), which is the largest thickness of tissues with which an effective signal can be detected from the tissue-covered SERS gels. According to this, we find that the maximum detection depth values range from 1–3 mm at the NIR-I window, from 3 to 6 mm at the NIR-II window.

Combining Eq. (1) and (3), SNR with tissue thickness of  $d$  (maximum detection depth) can be calculated:

$$SNR_d = SNR_0 \cdot e^{-\mu_{eff} \cdot d} + c = 3 \quad (4)$$

Which corresponds to  $d$  as

$$d = \frac{1}{\mu_{eff}} (\ln SNR_0 - \ln(3 - c)) \quad (5)$$

Here,  $\mu_{eff}$  is known (see Table 1), and  $c$  is close to 0, which can be obtained through fitting the exponential decay model in Fig. 3a and b. In this way, we could calculate relationship between the original SNR ( $SNR_0$ ) and the maximum detection depth ( $d$ ). In Fig. 3f and g, we plotted Eq. (5), revealing a clear relationship between the maximum detection depth versus the natural logarithm value of SERS gel SNR. The penetration is all improved at the NIR-II window for all tissues. Muscle remained the easiest penetrated tissue, and kidney is the hardest. This result provides important insights that the maximum detection depths are largely determined by two factors – the intrinsic optical properties of the tissue, and the overall SNRs of the system without the tissue (system SNR, a result of nanotag brightness, instrument efficiency, and data acquisition parameters).

It is interesting that in vivo SERS detection at the NIR-II window also benefits from the reduced auto-fluorescence from biological chromophores. We measured the Raman spectra under both excitations on seven types of tissues, i.e., skin, muscle, brain, lung, kidney, liver, and fat. The spectra without baseline corrections were displayed in Fig. 4. They were smoothed and normalized by laser power and integration time for better comparison. With 638 nm excitation, the Raman peaks are overwhelmed by the strong autofluorescence background. With 785 nm excitation, the fluorescence background is observed for all tissues, especially for the liver, kidney and brain due to the enrichment of hemoglobin and structural proteins in these tissues [30]. Some Raman characteristic peaks of the tissues are buried



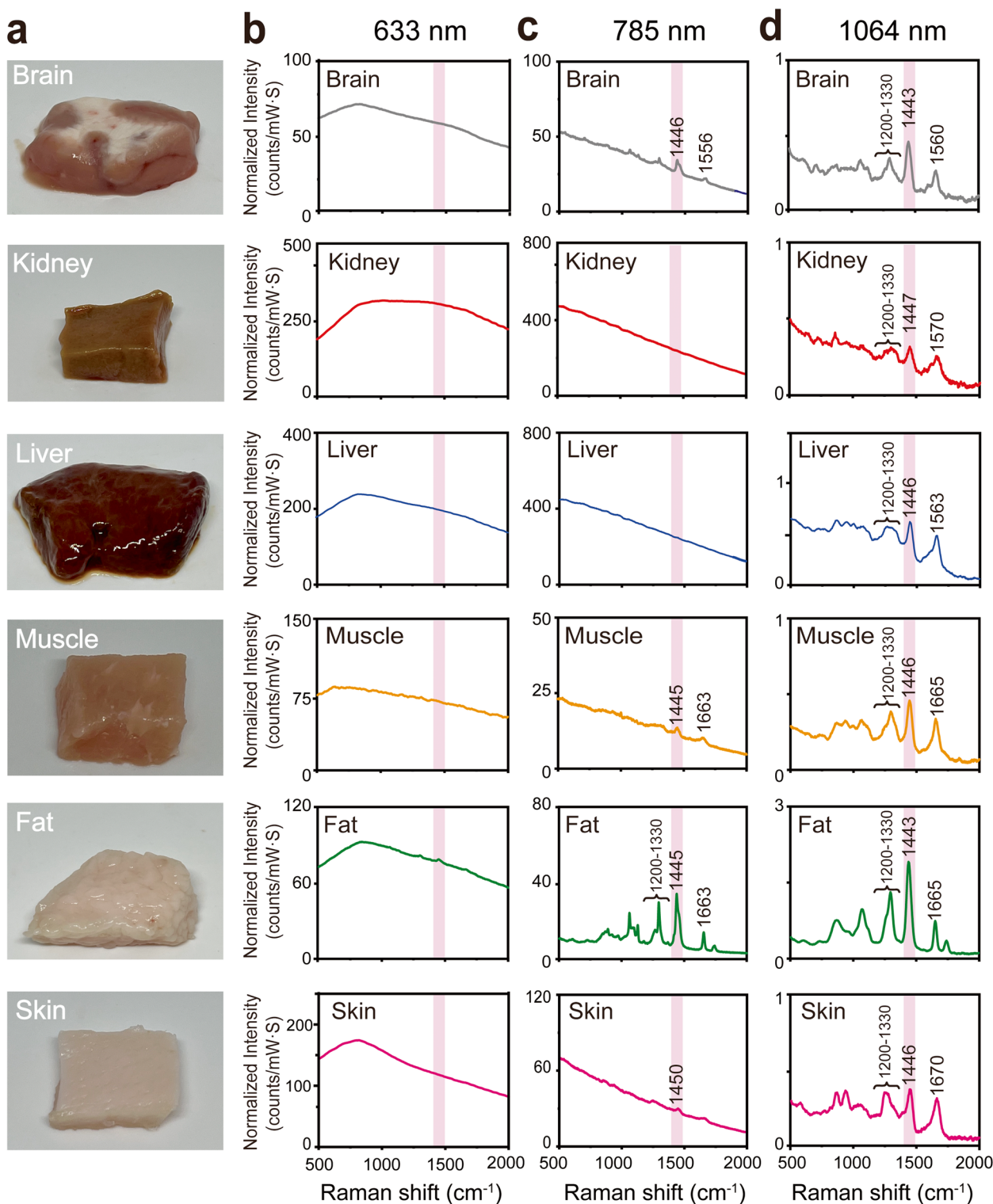


**Fig. 4** Wavelength-dependent tissue background interferences. **a** Bright-field image of tissues and **(b-d)** the original spectra collected at **(b)** 633, **(c)** 785, and **(d)** 1064 nm. The tissues are skin, muscle, brain, kidney, liver and fat. The measurements were performed under 633 nm (30 mW, 5 s integration time), 785 nm (200 mW, 0.5 s integration time), and 1064 nm (400 mW, 5 s integration time) excitation. The spectra intensities are normalized by the laser power and integration time. We chose the baseline value near 1445–1446  $\text{cm}^{-1}$  (marked by pink) to compare the normalized background intensity

**Table 2** Normalized tissue autofluorescence background intensity (counts/mW·s) at 1446  $\text{cm}^{-1}$ , under 633, 785 and 1064 nm excitation. Data were obtained from Fig. 4

Tissue types	633 nm	785 nm	1064 nm
Brain	58.3	25.8	0.16
Kidney	75	5	0.12
Liver	211.4	216	0.35
Muscle	311.1	236	0.13
Fat	69.7	11.5	0.11
Skin	117.9	26.8	0.11

in the background interference and hard to recognize, e.g., 1446 and 1653  $\text{cm}^{-1}$  peak in complex organs like liver and kidney. In contrast, all Raman peaks well emerged at 1064 nm excitation when tissue chromophore fluorescence decreases exponentially at longer wavelength [31]. Characteristic peaks in biological tissue samples include modes at 1445  $\text{cm}^{-1}$ , 1660  $\text{cm}^{-1}$ , and in the range of 1200–1330  $\text{cm}^{-1}$ , which correspond to the  $\text{CH}_2$  deformation peak, amine I band, and amine III band, respectively [32, 33]. These results provide an important insight for the in vivo SERS applications. The characteristic peaks of SERS NPs should be well discriminated with tissue background peaks for clear intraoperative imaging. The selected Raman reporter molecules are therefore preferred to have peaks within the region of 1100–1200  $\text{cm}^{-1}$ , 1500–1600  $\text{cm}^{-1}$  and particularly 1800–2200  $\text{cm}^{-1}$  (the biological-silent window) to avoid the overlaps with tissue Raman peaks.

We quantitatively calculated the baseline value near 1446  $\text{cm}^{-1}$  (indicated by pink in Fig. 4b). Since this peak is the characteristic Raman peak for most tissues, we use the intensity at the base of the peak for comparison. Considering that different measurements were applied for three wavelengths, we normalized the intensity by the laser power and integration time (counts/mW·s). As shown in Table 2, the background intensity ranges from 58.3 to 311.1 with 633 nm excitation, and decreases when the excitation wavelength moves to 785 nm. However, liver and kidney remained with high background interferences. When moving to the NIR-II window, all the background noises are dramatically reduced. This makes it possible for us to adopt longer exposure time at the NIR-II window. For instance, the background of kidney is extremely high under 633 and 785 nm excitation, and no clear Raman peaks are observed. In this case, it will be challenging for us to extend the integration time in order to get better SNR, since this may easily cause the saturation of charge-coupled device (CCD) detector. In contrast, the background intensity drops tremendously at 1064 nm excitation even with a longer integration time. This benefits in vivo SERS detections where an extended

collection time may be required compared to the common fluorescence imaging.

## Deciding factors on spectroscopic detection depth

With known relationship between the spectroscopic detection depth and SERS gel SNR, we continued to investigate the ways to enhance the detection depth at the NIR window. The following factors were considered for the investigations, including the measurement conditions (laser power and integration time) and signal source intensities. We chose muscle and fat tissues for investigation since they are most frequently dealt with in intraoperative studies; also, they are easy to obtain and prepare tissue slides. The wavelength of 785 nm excitation was applied. The measurements were firstly performed using a laser power of 5, 10, 50, 100, 200 mW with 10 s integration time. As shown in Fig. 5a, the SNR attenuation fits well by exponential decay curves ( $R^2$  of over 0.99). If we further compare different laser powers, it can be seen that SNR improves with increasing laser power, fitted well with power function models (Fig. S10). This coincides with the theoretical estimations that SNR is proportional to the squat of laser power for spectra of high intensities (see more details in the supporting information). We should note that although tissue attenuation coefficients are not related to laser power, the calculation process may be affected by a low laser power, which induces intense noises in the Raman spectrum and thus lead to biases in calculating SNR. For example, we have fitted the data in Fig. 5a on muscle tissues and calculated corresponding  $\mu_{\text{eff}}$  values (see Table S2). For the laser power of 50–200 mW, the fitted values of  $\mu_{\text{eff}}$  have no significant differences with previously obtained muscle  $\mu_{\text{eff}}$  ( $1.535 \pm 0.082$ ). While as the power decreases to 10 and 5 mW, the differences become larger. Therefore, we believe the measurements on  $\mu_{\text{eff}}$  should apply high-quality Raman spectra using adequately high laser powers.

The extension of integration time also plays an important role in improving signal penetration. We measured the SNR with a shorter integration time of 1 s and 5 mW power, the detection depth was reduced to less than 1 mm for all tissues. The highest detection depth obtained using 200-mW laser power and 10-s integration time was 6 and 3 mm for muscle and fat. When using a low laser power of 5 mW, the maximum detection depths dropped to 3 and 1 mm for muscle and fat.

The properties of the SERS gel directly determine the SNR of the measurements. Therefore, we have tuned SERS gels with different brightness (Fig. 5c). This is achieved by applying SERS NPs of different concentrations from 1 to 100 pM (see Fig. S2 for the photograph of the SERS gel). We have also discussed whether NP dose of these SERS gel are within a reasonable range (See Supporting Information).

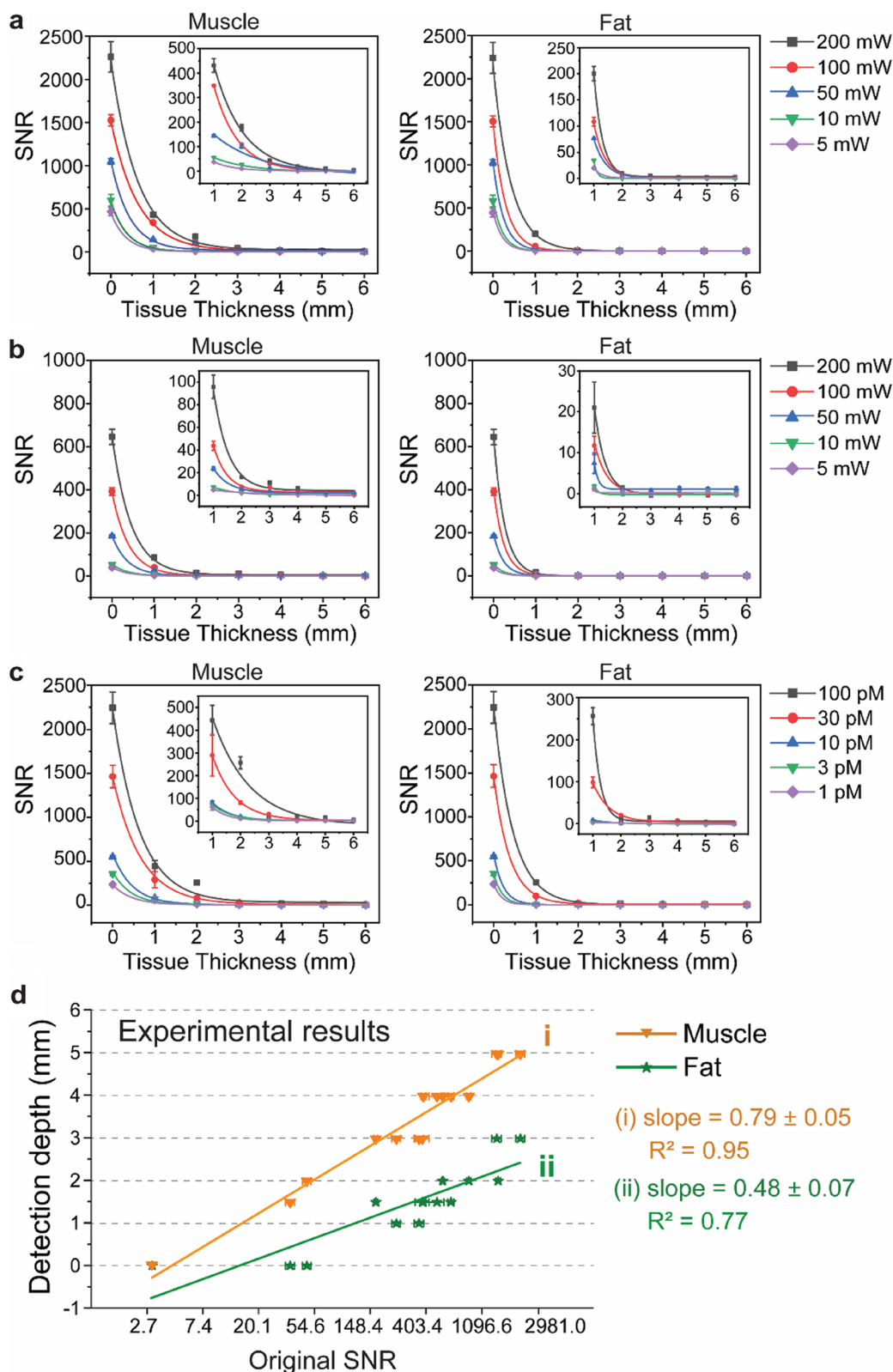


**Fig. 5** Comparison of the spectroscopic detection depths with varying SNRs of systems under 785 nm excitation. **a, b** Laser power-dependent SNR on muscle and fat tissues. The powers are 5, 10, 50, 100, 200 mW. The integration time is either 10 s (**a**) or 1 s (**b**). The SERS NP concentration is 100 pM. **c** SERS NP concentration dependent SNR on muscle and fat tissues. The NP concentration is 1, 3, 10, 30, and 100 pM. The power is 200 mW with 10 s integration time. The R-squares of the exponential fitting of the above curves are all over 0.99. **d** Relationship between the SNR of the system and the detection depth measured experimentally. The slopes and R-squares of linear fitting are displayed

The same measurement conditions were used as 200 mW and 10 s integration time. The SNR curve also shows an exponential decay in relation to tissue thickness ( $R^2$  of over 0.99). The increase in SERS gel intensities brought stronger signal peaks, leading to higher SNR. The lowest detection depths using the 10 pM gel were 3 and 1 mm for muscle and fat, respectively. The experimental results indicated that the improvement on the brightness of signal source could be a direct strategy to improve the detection depths.

We plotted the graph of detection depths versus the corresponding SERS gel SNR measured in the above experiments (Fig. 5d). A clear linear-logarithmic relationship between the two is revealed for each tissue. For fitting, the point (3, 0) was included, representing an original SNR of 3 and the detection depth as zero. It can be seen that, although the intercepts are shifted, the experimental results are close to the theoretical calculations in Fig. 3f. For muscle tissues, the slope is  $0.79 \pm 0.05$ , corresponding to an attenuation coefficient in a range of 1.19–1.35; For fat tissues, the slope is  $0.48 \pm 0.07$ , corresponding to the attenuation coefficient in a range of 1.81–2.43. The result confirms that the spectroscopic detection depth is determined by SNR of the system, i.e., the SNR of SERS gels without the tissues covered. Here, system SNR is a result of nanotag brightness, instrument efficiency, and data acquisition parameters.

The above theoretical and experimental results provide a generalized linear-logarithmic relationship between system SNR and spectroscopic detection depth. The slope and intercept of this relationship are determined by the tissue properties. Although we only used SERS NPs with 4-NBT molecules in this work, similar trends could be expected for other Raman reporters, Raman NPs, or non-Raman agents. This result opens the possibility of predicting the penetration performance of optical contrast agents in clinical applications. For example, one could estimate the thickness of tissue covered on agent-labeled lesions to calculate the SNR required for successful detection. This can help to (1) determine the injection dose by considering the targeting efficiency and the brightness of the imaging agent measured in vitro, or (2) guide the design of imaging agents by deciding whether the imaging agents are bright enough when determining the injection dose. For different tissues, we assume different penetration depth and SNR due to their different optical properties. When it comes to in vivo environments, the intercept or slope values of our model should be adjusted for several reasons: The first is the more complicated in vivo environment, which leads to multiple reflection and refraction effects at tissue interfaces. The second is the different optical properties between SERS gel and real lesions. For example, the reflectance at the interfaces between agarose gel and ex vivo tissues in this study may slightly decrease the SNR. The third is the dynamic changes such as blood flow. We assume that this can be

mimicked using a theoretical model with slightly different optical attenuation coefficients. Overall, our study provides the method to assess the penetration performance of imaging agents and benefit their translation to in vivo scenarios.

### Spectroscopic detection depth study using fluorescence spectroscopy

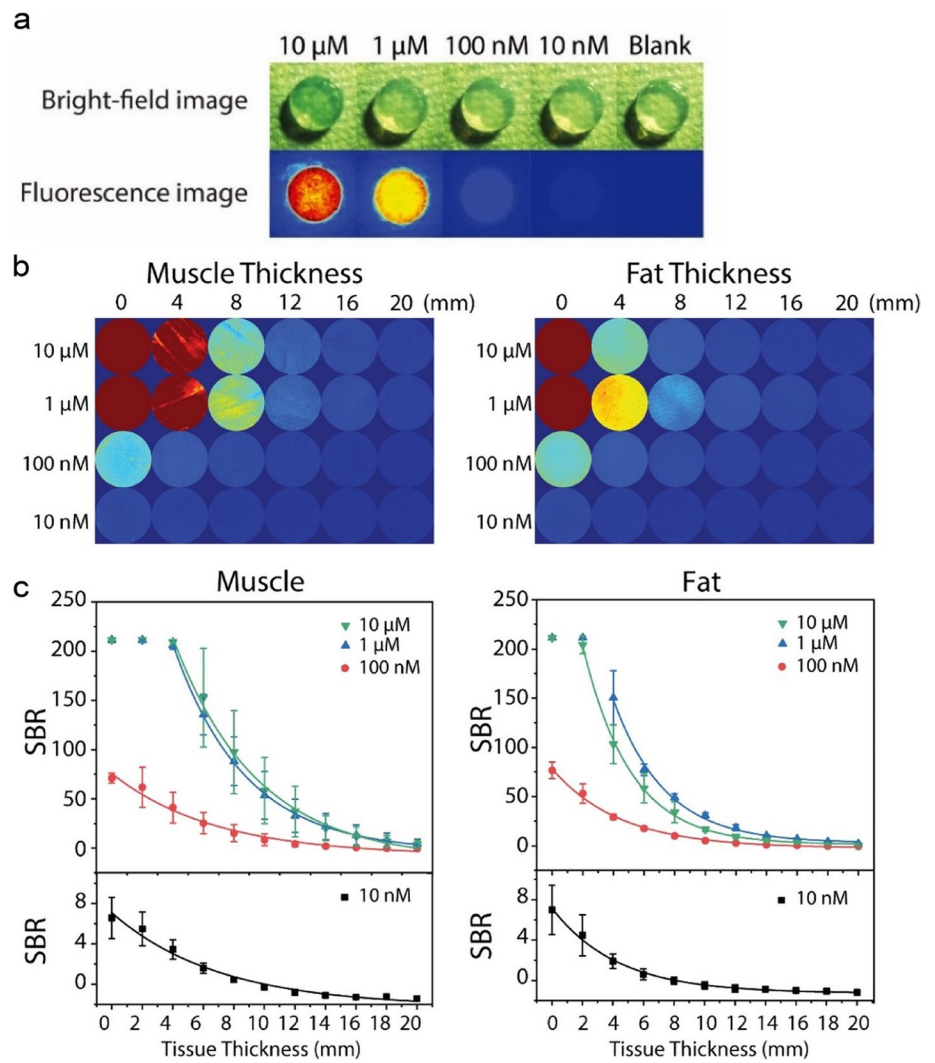
The concepts and setup presented in this work are not restricted to SERS but applicable to many spectroscopy-based techniques. We additionally performed the penetration assessment using fluorescence imaging, which provides a significant reference for the clinical practices since it has been widely used in surgical guidance with the ability to offer real-time visualizations on a large area of interests. The fluorescence images were captured by a wide-field NIR camera of the image-guided surgery system (Fig. S11). Therefore, we used the SNR of the fluorescence images to evaluate the corresponding detection depth. The image SNR was defined as the difference between the average fluorescence intensities of sample images and background over the standard deviation of the background intensities, as mathematically stated by the equation:

$$SNR = \frac{I_{signal} - I_{Background}}{\sigma_{Background}} \geq 3 \quad (6)$$

The pure agarose gel was adopted as the blank sample to provide a background reference, whose image intensity deviations were applied as background noise. The NIR fluorophore indocyanine green (ICG) was adopted and a series of ICG gels was prepared with the ICG concentration to be 10 nM, 100 nM, 1  $\mu$ M, and 10  $\mu$ M (Fig. 6a). The ICG gels were then covered by tissues of 2 to 20 mm for the penetration assessment. The fluorescence images gave both qualitative and quantitative information about the effect of tissue thickness and ICG concentration on fluorescence intensity (Fig. 6b). An overall trend of intensity decay over increasing tissue thickness was revealed on all ICG gels. The profile of intensities versus tissue thickness was fitted well by exponential decay curves. The maximum detection depth was defined as the largest thickness via which a statistically significant fluorescence signal could be detected. As shown in Table S3, the highest detection depth obtained when the ICG concentration increased to 1  $\mu$ M, the results were improved to 20 and 18 mm for muscle and fat, respectively. For 10  $\mu$ M gel, the detection depths were slightly decreased, turned out to be 20 and 16 mm for muscle and fat. The SNR curve of 10 and 1  $\mu$ M overlapped with large standard deviations, indicating they were at the same level. The failure to show improvements in penetration for 10  $\mu$ M gel might be related to the increasing photobleaching rate for higher-concentration fluorophores. This result may suggest a suitable ICG



**Fig. 6** Spectroscopic detection depth assessments using fluorescence. **a** Bright-field and fluorescence images (pseudocolor heat map) of ICG gels. The gel samples included ICG concentrations of 10  $\mu\text{M}$ , 1  $\mu\text{M}$ , 100 nM and 10 nM as well as a blank agarose gel. The fluorescence images reveal an overall trend of fluorescence intensity decay with respect to the decreased ICG concentration. **b** Fluorescence images (pseudocolor heat map) of ICG gels covered by muscle and fat tissues of 0–20 mm. **c** The decay of image SNR as a function of tissue thickness on ICG gels with different concentrations on muscle and fat tissues. Note that the fluorescence signals of 1 and 10  $\mu\text{M}$  ICG gels were saturated with their measured intensity as 255 reaching the threshold, so these points were excluded in the fitting. The R-squares of the exponential fitting of the above curves are all over 0.97



concentration of no more than 1  $\mu\text{M}$  is for practical usage to avoid severe photobleaching effects.

Whether SERS is better than fluorescence from the perspective of detection depth remains a controversial topic. Although, in this work, the highest detection depths on fluorescence are of 20 and 18 mm for muscle and fat, higher than that of Raman spectroscopy, we should note that it is not a direct comparison between SERS and fluorescence, because their instruments and measurement conditions are very different: the integration time of fluorescence is short, restricted by the photobleaching of fluorophores; and SERS usually adopts the higher integration time and a point-scanning method, which is restricted by the low cross-section of Raman spectroscopy. By using fiber-optic instruments and brighter SERS NPs, the maximum detection depths of SERS could be over that of fluorescence, as we demonstrated previously [21]. Overall, since fluorescence has been widely used to offer real-time visualizations of a large area during open

surgeries, our ex vivo results of its detection depth offer a significant reference for clinical practices.

## Conclusion and discussion

We have presented the concept and conducted the quantitative assessments of tissue attenuation and spectroscopic detection depth at the NIR window. Based on data from six types of fresh ex-vivo tissues (brain, kidney, liver, muscle, fat and skin), we obtain the spectroscopic detection depth values range from 1–3 mm in the first NIR window, from 3 to 6 mm in the second NIR window. The results match with the previous reports in a wide range of hundreds of micrometers to several millimeters [3, 12]. We further demonstrate the reduced tissue attenuation coefficients and autofluorescence interference at 1064 nm. Under 785 nm excitation, the normalized SNR is attenuated by 80–93% with 1-mm tissue; As for the 1064 nm excitation,

the corresponding attenuation is reduced to 66–85%. The penetration of muscle and liver is the highest, followed by kidney and brain. Fat and skin remain the most turbid tissues for both wavelengths.

By using SERS and fluorescence, we show that the intrinsic optical properties of the tissue and the system SNR are the two deciding factors of signal penetration in bio-tissues. In particular, our theoretical and experimental demonstrations provide a generalized linear-logarithmic relationship between the system SNR and spectroscopic detection depth for each tissue. Thus, the detection of hidden lesions can be improved by two strategies – minimizing tissue attenuation and background noise, and maximizing the system's performance as judged by SNR. Considering that the tissue optics are intrinsic properties, and the measurement conditions are usually restricted in medical procedures, the only factor that can be largely improved is the nanotag brightness intensity. This reasonably explains why a significant number of studies has been reported on the invention of ultra-bright contrast agents [23]. Therefore, though the maximum detection depths obtained in this work were limited in the a few millimeters, we anticipate better depth detection ability by developing brighter SERS nanotags in the future. Also, our assessment method can be applied to the detections by deep Raman techniques, which have reported to achieve the detection depths of a few centimeters [34–36].

Overall, our study offers a straightforward method to evaluate the performance of optical contrast agents and their detection limits in tissues. This work also benefits future investigations on a variety of non-Raman contrast imaging agents such as fluorescent dyes, up-conversion NPs, organic semiconductors, etc. We anticipate that the comprehensive combination of innovations in imaging agents and detector systems will constitute the radical advances for in vivo optical detection, spectroscopic wearable devices, and deep-tissue intraoperative imaging in practical applications.

## Materials and Methods

### Materials

All chemicals were used as received without any further purification. Cetyltrimethylammonium chloride (CTAC,  $\geq 99.0\%$ ), sodium borohydride ( $\text{NaBH}_4$ , 98%), chloroauric acid tetrahydrate ( $\text{HAuCl}_4 \cdot 4\text{H}_2\text{O}$ ), 4-nitrobenzenethiol (4-NBT), bovine serum albumin (BSA), dimethyl sulfoxide (DMSO), phosphate-buffered saline (PBS) and ascorbic acid were purchased from Sigma-Aldrich. Phosphate-buffered saline (PBS) was purchased from Corning. Silver nitrate ( $\text{AgNO}_3$ , 99.8%) was purchased from Aladdin (China). Indocyanine green (ICG) was purchased from TCI America. Agarose was purchased from Fisher Scientific. De-ionized water was used in all experiments.

### Ex vivo porcine tissues

The fresh ex vivo porcine tissues were purchased from grocery stores and frozen before use. The adopted tissues included muscle, skin, fat, liver, bone, lung, and kidney. Specifically, the pork tenderloin was chosen for muscle samples, and side pork for skin and fat samples. The skin samples were composed of  $\sim 1$  mm skin layers and subcutaneous fat layers. A meat slicer was applied to cut the frozen muscle, fat, and skin tissues into thin layers with different thicknesses. The length and width of tissues were over 3 cm to fully cover the SERS gel. A vernier caliper was adopted to measure the thickness of each slice. Considering the softness of tissue samples, a 5–10% deviation in thickness was acceptable.

### Preparation of SERS nanoparticles and SERS gels

SERS NPs were synthesized using our reported method [21]. The Au core colloids (1 nM) were firstly prepared using a seed-mediated method [22]. 4-NBT was used as the Raman reporters. Then 500  $\mu\text{L}$  of 4-NBT ethanol solution (10 mM) was mixed with 10 mL of Au core colloids under vigorous sonication. After 0.5 h, the colloids were centrifuged and washed with CTAC aqueous solution (50 mM) to remove excess 4-NBT molecules. Then 1 mL of 4-NBT modified cores were added into the mixture of 16 mL of CTAC solution (50 mM), 480  $\mu\text{L}$  of ascorbic acid (40 mM), and 960  $\mu\text{L}$  of  $\text{HAuCl}_4$  (4.86 mM). The products (0.049 nM) were collected after the 10-min reaction. After that, the colloids (0.6 nM) were added to a mixture of 2.5 mL CTAC (25 mM), 400  $\mu\text{L}$   $\text{AgNO}_3$  (14.58 mM) and 1.875 mL ascorbic acid (40 mM). The mixture was then reacted in a 70 °C water bath for 3 h. Finally, the products were washed with CTAC (50 mM) twice to remove excess molecules and redispersed in CTAC aqueous solution (50 mM). The products were characterized by the UV-Vis spectrometer (Aucybest, China) and the transmission electron microscopy (JEOL JME-2100F, Japan).

For the preparation of SERS gels, the obtained SERS NP colloids were washed by water twice to remove excess CTAC, then redispersed in water with the NP concentration of 2 nM. Then 1 wt% agarose aqueous solution was heated up in a microwave oven until the turbid solution turns clear. We mixed 1.9 ml of agarose solution with 0.1 ml of SERS colloids, to get the final NP concentration of 0.1 nM. As the mixture was in a liquid phase with a high temperature, the colloids were sonicated to ensure that the NPs were well dispersed. Then 2 mL of mixtures were quickly transferred into the wells of a 12-well plate. The slight shaking and swirling were applied to ensure that the mixture was well dispersed. Let sit at room temperature for 1 h, until the agarose gel cooled down and was completely solidified. The SERS gel

was carefully removed out of the 12-well plate. The SERS gel was finally obtained with a thickness of around 1 cm.

### SERS measurement setup

For the SERS measurements, the 785/1064 dual-mode hand-held Raman spectrometer (Antonpar) and its matching optical XYZ-linear stage were applied for muscle, fat and skin tissues. The spectral resolution was  $\sim 2 \text{ cm}^{-1}$  for 785 nm and  $\sim 11 \text{ cm}^{-1}$  for 1064 nm measurement. For the liver, kidney and brain tissues, the spectrometer was changed due to the machine maintenance. We applied the BWTEK i-Raman spectrometer (BWS475-785S-HT, BWTEK, USA) for 785 nm excitation, and the Oceanhood hand-held spectrometer (Portman PR1064, Shanghai Oceanhood Optoelectronics Tech Co., LTD, China) for 1064 nm excitation. The focal length and focal depth were measured as follows [37]: a silicon wafer was placed on the stage platform, then the sequential acquisition of Raman spectra was performed when keeping the laser probe stationary and moving the platform up and down vertically with a step of 0.2 mm. The intensity of  $520 \text{ cm}^{-1}$  mode of the silicon wafer was used to calculate the SNR. Take the dual-mode hand-held Raman spectrometer (Antonpar) for example, the plotted SNR-distance profile was a curve of Gaussian distribution with a decrease in both sides of the ideally focal plane (Figure S2). For the optimization in the focal plane, the laser probe was fixed on top of the stage, and the SERS gel was placed on the glass substrate at the stage platform. The frozen porcine tissues were sliced into thin layers of 1 - 6 mm, put above the SERS gel to fully cover it, ensuring no air bubble in-between. The sequential acquisitions of Raman spectra on tissue-covered SERS gels were performed when moving the optical stage in the z-direction. The data were recorded at different z values from -6 mm to +7 mm with a step of 0.756 mm. These obtained best focus positions were adopted for the SERS penetration assessments.

### Raman measurements on tissue autofluorescence background

For the Raman measurements on tissue autofluorescence background, we applied three hand-held spectrometers: for 633 nm excitation, we used Oceanhood hand-held spectrometer (Portman, Shanghai Oceanhood Optoelectronics Tech Co., LTD, China) with 1.63 mW and 5 s integration time; for 785 nm excitation, we applied BWTEK i-Raman spectrometer (BWS475-785S-HT, BWTEK, USA) with 200 mW, 0.5 s integration; for 1064 nm excitation, we applied Oceanhood hand-held spectrometer (Portman PR1064, Shanghai Oceanhood Optoelectronics Tech Co., LTD, China) with 400 mW and 5 s integration time.

### Raman spectra analysis

The baselines of raw spectra were corrected using the adaptive iteratively reweighted Penalized Least Squares (airPLS) algorithm to remove the tissue autofluorescence background while preserving characteristic Raman peaks. The spectra were smoothed using a moving window average algorithm with a window size of 5. We do not use peak fitting as the peak positions of SERS nanoparticles are known. The intensities of signal peak ( $1338 \text{ cm}^{-1}$ ) are calculated by averaging the data in the range of  $1338 \pm 6 \text{ cm}^{-1}$ ; while the noise is the standard deviation in the region of  $2100 \pm 100 \text{ cm}^{-1}$ .

For a mixed Raman signal collected from SERS gels and tissues, we directly calculated the tissue signal and then subtracted it from the mixed spectrum, since the signals from NPs and tissues are determined. Figure S5 shows an example of a mixed Raman spectrum collected from SERS gels covered by muscle tissues (785 nm excitation). The signal exhibits contributions from both gel and muscle. The peak at  $1338 \text{ cm}^{-1}$  of SERS gel was distinguishable yet of a slight overlap with tissue peak, so a simple subtraction of tissue contribution is performed to extract a real value of  $I_{1338}$  based on the intensity ratio of two peaks: since  $1445 \text{ cm}^{-1}$  mode in the mixed spectrum is mainly contributed by the muscle, once knowing the ratio of  $1338 \text{ cm}^{-1}$  to  $1445 \text{ cm}^{-1}$  for muscle tissues, their contribution at  $1338 \text{ cm}^{-1}$  can be calculated and determined. This intensity ratio value may slightly vary for different batches of porcine tissues, so this calibration should be conducted each time before the data analysis. We measured at least 10 spectra for each batch. For example, a typical intensity ratio of  $1338 \text{ cm}^{-1}$  ( $1338 \pm 6 \text{ cm}^{-1}$ ) to  $1445 \text{ cm}^{-1}$  ( $1445 \pm 8 \text{ cm}^{-1}$ ) is calculated as  $0.36 \pm 0.06$  for muscle, so the signal intensity is modified as  $I_{1338} - 0.36 \times I_{1445}$ . Similar procedures were done for all the rest tissues. For fat, skin, brain, kidney and liver tissues, the ratios are  $0.09 \pm 0.007$ ,  $0.35 \pm 0.10$ ,  $0.30 \pm 0.04$ ,  $0.55 \pm 0.04$ ,  $0.50 \pm 0.02$ , respectively (displayed as mean  $\pm$  SD). Nevertheless, we would like to note for kidney or brain tissues that have little Raman response near  $1338 \text{ cm}^{-1}$ , it does not make a big difference with or without the subtraction.

### Fluorescence penetration measurement

The ICG gels were prepared using a similar protocol to the SERS gels. First, ICG was dissolved in DMSO to prepare a 1 mM stock solution. The stock solution was further diluted by 10 mM PBS buffer (with 0.1 mM bovine serum albumin) to prepare a series of ICG solutions from 100  $\mu\text{M}$  to 10 nM. Then 2.7 mL of agarose aqueous solution (1 wt%) were mixed with ICG solutions in a 9:1 v/v ratio. The mixtures were transferred to a 12-well plate and solidified at room

temperature to form the ICG-agarose gels. The imaging was carried out by a NIR-I fluorescence image-guided surgery system (REAL-IGS, LIFENERGY Nanjing Nuoyuan Medical Devices, China) optimized for ICG fluorescence detection in medical use (shown in Figure S5). The imaging system consists of a 785 nm planar laser as the excitation source and a NIR-I camera. ICG gel was placed on the platform with tissues on top. The frozen porcine tissues were sliced into thin layers of 2 mm, constructing tissue thickness ranging from 2 mm to 20 mm. The uniform planar laser illuminated an area of 10 cm×10 cm with the working distance of the laser probe to the samples as 50 cm. The laser output power was set as 480 mW with the power density at the sample of around 4.5 mW/cm<sup>2</sup>. The shutter time was 792 μs. The pure agarose gel was adopted as the blank sample, whose image intensity deviations were applied as background noise. We calculated the temporal noises from a series of images on agarose gel.

When imaging the pure ICG gel without tissues on top, the camera gain was 350 for better contrast; when imaging the ICG gels with tissues, the camera gain was adjusted to the maximum of 593 for the better penetration performance. The captured grayscale fluorescence images were further processed by ImageJ and MATLAB (Mathworks) to display a pseudocolor heatmap for visualization. The intensity of each image was read from the region of interest (ROI) that was carefully selected as a circle with a diameter of 350 pixels. The circle was slightly smaller than the gel area and leaving a 0.5 - 1 cm margin to reduce the effects of the glowing edges.

**Supplementary Information** The online version contains supplementary material available at <https://doi.org/10.1007/s44258-023-00010-2>.

**Authors' contributions** L. Lin established the methodology. L. Lin, H. He, and R. Xue conducted the SERS assessments and related data analysis. Z. Wang conducted the fluorescence assessments and related data analysis. L. Lin, H. He, and Y. Zhang prepared the nanomaterials. L. Lin and Y. Zhang conducted the theoretical calculations. J. Ye provided the initial ideas and the setups. S. Nie conceptualized this project and devised the proof of outline. L. Lin wrote the original manuscript, which was reviewed and revised by all authors. All authors read and approved the final manuscript.

**Funding** This work was supported by National Natural Science Foundation of China (Nos. 82272054 and 81901786), the Science and Technology Commission of Shanghai Municipality (No. 21511102100), Innovation Research Plan supported by Shanghai Municipal Education Commission (No. ZXWF082101). S.N. acknowledges insightful discussions with Dr. Sunil Singhal of the University of Pennsylvania, the US National Institutes of Health (grant 1P01 CA254859) and the University of Illinois at Urbana-Champaign. This work was also supported by China Postdoctoral Science Foundation (No. 2019T120343), Shanghai Jiao Tong University (Nos. YG2019QNA28 and YG2022QN006), and Shanghai Key Laboratory of Gynecologic Oncology. L. L. also acknowledges "Chenguang Program" supported by Shanghai Education Development Foundation and Shanghai Municipal Education Commission (21CGA09).

**Availability of data and materials** All data needed to support the conclusions of this study are available within the article and its supplementary materials or at request from the authors.

## Declarations

**Competing interests** The authors declare that there is no conflict of interest regarding the publication of this article. Author Shuming Nie is an Associate Editor for Med-X. The paper was handled by another Editor and has undergone a rigorous peer review process. Author Shuming Nie was not involved in the journal's peer review of, or decisions related to, this manuscript.

**Open Access** This article is licensed under a Creative Commons Attribution 4.0 International License, which permits use, sharing, adaptation, distribution and reproduction in any medium or format, as long as you give appropriate credit to the original author(s) and the source, provide a link to the Creative Commons licence, and indicate if changes were made. The images or other third party material in this article are included in the article's Creative Commons licence, unless indicated otherwise in a credit line to the material. If material is not included in the article's Creative Commons licence and your intended use is not permitted by statutory regulation or exceeds the permitted use, you will need to obtain permission directly from the copyright holder. To view a copy of this licence, visit <http://creativecommons.org/licenses/by/4.0/>.

## References

1. Son D, et al. Multifunctional wearable devices for diagnosis and therapy of movement disorders. *Nat Nanotechnol.* 2014;9(5):397–404.
2. Welsher K, Sherlock SP, Dai H. Deep-tissue anatomical imaging of mice using carbon nanotube fluorophores in the second near-infrared window. *Proc Natl Acad Sci U S A.* 2011;108(22):8943–8.
3. Hong G, Antaris AL, Dai H. Near-infrared fluorophores for biomedical imaging. *Nat Biomed Eng.* 2017;1(1):0010.
4. Hu Z, et al. First-in-human liver-tumour surgery guided by multispectral fluorescence imaging in the visible and near-infrared-II windows. *Nat Biomed Eng.* 2020;4(3):259–71.
5. Zhu S, et al. Molecular imaging of biological systems with a clickable dye in the broad 800- to 1,700-nm near-infrared window. *Proc Natl Acad Sci U S A.* 2017;114(5):962–7.
6. Hong G, et al. Through-skull fluorescence imaging of the brain in a new near-infrared window. *Nat Photonics.* 2014;8(9):723–30.
7. Kircher MF, et al. A brain tumor molecular imaging strategy using a new triple-modality MRI-photoacoustic-Raman nanoparticle. *Nat Med.* 2012;18(5):829–34.
8. Xie HN, et al. Tracking bisphosphonates through a 20 mm thick porcine tissue by using surface-enhanced spatially offset Raman spectroscopy. *Angew Chem Int Ed Engl.* 2012;51(34):8509–11.
9. Mosca S, et al. Determination of inclusion depth in ex vivo animal tissues using surface enhanced deep Raman spectroscopy. *J Biophotonics.* 2020;13(1):e201960092.
10. Asiala SM, et al. Surface-Enhanced, Spatially Offset Raman Spectroscopy (SESORS) in Tissue Analogues. *ACS Appl Mater Interfaces.* 2017;9(30):25488–94.
11. Shan B, et al. Near-Infrared II Plasmonic Au@ Au-Ag Dot-in-Cubic Nanoframes for In Vivo Surface-Enhanced Raman Spectroscopic Detection and Photoacoustic Imaging. *Adv Func Mater.* 2021;31:2103186.



12. Lane LA, Xue R, Nie S. Emergence of two near-infrared windows for in vivo and intraoperative SERS. *Curr Opin Chem Biol.* 2018;45:95–103.
13. Nicolson F, et al. Non-invasive In Vivo Imaging of Cancer Using Surface-Enhanced Spatially Offset Raman Spectroscopy (SESORS). *Theranostics.* 2019;9(20):5899–913.
14. Lane LA, et al. SERS Nanoparticles in Medicine: From Label-Free Detection to Spectroscopic Tagging. *Chem Rev.* 2015;115(19):10489–529. <https://doi.org/10.1021/acs.chemrev.5b00265>.
15. Lin L, Xue R, Nie S. Surface-enhanced Raman scattering (SERS) nanoparticles for biodiagnostics bioimaging and spectroscopy-guided cancer surgery. In: Yin Y, Lu Y, Xia Y, editors. *Encyclopedia of Nanomaterials.* Elsevier. 2023. p. 340–355.
16. Davis RM, et al. Surface-Enhanced Raman Scattering Nanoparticles for Multiplexed Imaging of Bladder Cancer Tissue Permeability and Molecular Phenotype. *ACS Nano.* 2018;12(10):9669–79.
17. Lin L, et al. Surface-enhanced Raman scattering nanotags for bioimaging. *J Appl Phys.* 2021;129(19):191101.
18. Zhang Y, et al. Ultraphotostable mesoporous silica-coated gap-enhanced Raman tags (GERTs) for high-speed bioimaging. *ACS Appl Mater Interfaces.* 2017;9(4):3995–4005.
19. He H, et al. Resonant Strategy in Designing NIR-II SERS Nanotags: A Quantitative Study. *J Phys Chem C.* 2022;126(30):12575–81.
20. Li L, et al. Near-infrared II plasmonic porous cubic nanoshells for in vivo noninvasive SERS visualization of sub-millimeter microtumors. *Nat Commun.* 2022;13(1):5249.
21. Wu Z, et al. Raman-Guided Bronchoscopy: Feasibility and Detection Depth Studies Using Ex Vivo Lung Tissues and SERS Nanoparticle Tags. *Photonics.* 2022;9(6):429.
22. Lin L, Gu H, Ye J. Plasmonic multi-shell nanomatryoshka particles as highly tunable SERS tags with built-in reporters. *Chem Commun.* 2015;51(100):17740-3.
23. Khlebtsov NG, et al. Gap-enhanced Raman tags: fabrication, optical properties, and theranostic applications. *Theranostics.* 2020;10(5):2067–94.
24. Skadtchenko BO, Aroca R. Surface-enhanced raman scattering of p-nitrothiophenol molecular vibrations of its silver salt and the surface complex formed on silver islands and colloids. *Spectrochim Acta A Mol Biomol Spectrosc.* 2001;57A(5):1009–16.
25. Keiser G. Light-Tissue Interactions. In: *Biophotonics. Graduate Texts in Physics.* Singapore: Springer. 2016. p. 147–196. [https://doi.org/10.1007/978-981-10-0945-7\\_6](https://doi.org/10.1007/978-981-10-0945-7_6).
26. Ntziachristos V. Going deeper than microscopy: the optical imaging frontier in biology. *Nat Methods.* 2010;7(8):603–14.
27. Mosca S, et al. Optical characterization of porcine tissues from various organs in the 650–1100 nm range using time-domain diffuse spectroscopy. *Biomed Opt Express.* 2020;11(3):1697–706.
28. Lai P, Xu X, Wang LV. Dependence of optical scattering from Intralipid in gelatin-gel based tissue-mimicking phantoms on mixing temperature and time. *J Biomed Opt.* 2014;19(3):35002.
29. Jacques SL. Optical properties of biological tissues: a review. *Phys Med Biol.* 2013;58(11):R37–61.
30. Epstein JB, Sciubba JJ. Chapter 4 - Strategies for Oral Cancer Detection. In: Koch WM, editor. *Early Diagnosis and Treatment of Cancer Series: Head and Neck Cancers.* Philadelphia: Elsevier; 2010. p. 45–58.
31. Diao S, et al. Biological imaging without autofluorescence in the second near-infrared region. *Nano Res.* 2015;8(9):3027–34.
32. Rivas-Arancibia S, et al. Structural Changes of Amyloid Beta in Hippocampus of Rats Exposed to Ozone: A Raman Spectroscopy Study. *Front Mol Neurosci.* 2017;10:137.
33. Thomas G, et al. Evaluating feasibility of an automated 3-dimensional scanner using Raman spectroscopy for intraoperative breast margin assessment. *Sci Rep.* 2017;7(1):13548.
34. Zhang Y, Lin L, Ye J. A rapid and universal method for depth estimation of lesions in heterogeneous tissues via photosafe ratiometric transmission Raman spectroscopy. *VIEW.* 2023. p. 20230022.
35. Zhang Y, et al. In Vivo Surface-Enhanced Transmission Raman Spectroscopy under Maximum Permissible Exposure: Toward Photosafe Detection of Deep-Seated Tumors. *Small Methods.* 2023;7(2):2201334.
36. Wu Z, et al. Non-Invasive Detection Precise Localization and Perioperative Navigation of In Vivo Deep Lesions Using Transmission Raman Spectroscopy. *Adv Sci.* 2023. p. 202301721.
37. Cai W, et al. Application of the wavelet transform method in quantitative analysis of Raman spectra. *J Raman Spectrosc.* 2001;32(3):207-9.

**Publisher's Note** Springer Nature remains neutral with regard to jurisdictional claims in published maps and institutional affiliations.